THE ASTROPHYSICAL JOURNAL, 346:997–1009, 1989 November 15

ABUNDANCES OF ULTRAHEAVY ELEMENTS IN THE COSMIC RADIATION: RESULTS FROM *HEAO 3*

W. R. BINNS,[1] T. L. GARRARD,[2] P. S. GIBNER,[2] M. H. ISRAEL,[1] M. P. KERTZMAN,[3,4]
J. KLARMANN,[1] B. J. NEWPORT,[2,5] E. C. STONE,[2] AND C. J. WADDINGTON[3]

Received 1989 February 21; accepted 1989 May 12

ABSTRACT

We report here an analysis that, for the first time, systematically normalizes the data from the *HEAO 3* Heavy Nuclei Experiment on the cosmic-ray abundances of all the elements heavier than germanium to that of iron. In the range of atomic number Z, $33 \leq Z \leq 60$, the analysis yields abundances of odd-even element pairs. These abundances are consistent with a cosmic-ray source having a composition similar to that of the solar system, but subject to source fractionation correlated with the first ionization potential (FIP) of each element. For $Z > 60$, the analysis yields abundances of element groups. For these heaviest nuclei, we find an enhancement of the abundance of the platinum group, elements with $74 \leq Z \leq 80$, relative to that in a propagated solar system source, and a corresponding increase in the abundance of the largely secondary elements in the range $62 \leq Z \leq 73$. These abundances suggest that there is an enhancement of the r-process contribution to the source nuclei in the $Z > 60$ charge region. Over the entire region of charge, standard leaky box models of propagation satisfactorily model secondary production.

Subject headings: cosmic rays: abundances — nucleosynthesis

I. INTRODUCTION

The study of ultraheavy (UH) nuclei in the cosmic radiation (those with atomic number $Z \geq 30$) addresses several important questions of astrophysical interest. Abundances of cosmic-ray nuclei can be compared to specific predictions of nucleosynthesis processes to look for the signatures of various production mechanisms. For UH nuclides, neutron capture is the dominant process of nucleosynthesis, and may be modeled in terms of two extremes. A slow process (s-process), which permits β-decay before additional neutron captures, occurs in some stages (e.g., red giant) of the evolution of normal stars. A rapid process (r-process), resulting in multiple neutron captures before β-decay, would be characteristic of extreme environments, such as those in supernovae. The neutron capture cross sections and the systematics of the β-decay, which are well understood for the s-process and less well understood for the r-process, lead to distinct differences in predicted elemental abundance distributions.

Measurements of the abundances of UH nuclei are also important in the study of propagation of cosmic rays through the interstellar medium. The standard leaky box model for propagation of cosmic rays through the Galaxy is principally characterized by the mean free path for escape from the trapping volume, expressed as a function of the rigidity of the nuclei. Since the UH nuclei have much shorter mean free paths for nuclear interactions than the lighter elements do, they are more likely to interact before escaping, and are thus less sensitive to the escape mean free path, providing a different perspective on propagation models. Many of the elemental abundances reported here have substantial contributions of secondary nuclei (i.e., nuclei produced as secondary fragments of heavier nuclei by nuclear interactions in the interstellar medium, rather than having been injected as primary nuclei at the cosmic-ray source), and hence are relatively good tracers of the propagation process.

In this paper, we report a measurement of UH elemental abundances for $Z > 32$ normalized to the abundance of iron, $_{26}$Fe. We have analyzed the entire charge region from $Z \sim 20$ to the heaviest elements in a uniform manner, so that comparisons may be made across large differences in Z. In this analysis, as in our previous analyses over more limited ranges of Z (Binns *et al.* 1981*a*, 1982, 1983*a*, *b*, 1985; Stone *et al.* 1983), it has been necessary to compromise between resolution and number of events when selecting particles for inclusion. The data set discussed here results from a selection with an intermediate geometry factor and intermediate resolution compared to the earlier analyses. The selection parameters have been chosen to allow clear resolution of the more abundant, even-Z elements over much of the charge interval, while yielding a statistically meaningful measurement of the low abundances in the charge intervals $40 \leq Z \leq 49$ and $62 \leq Z \leq 74$. This good resolution is particularly important in regions such as $38 \leq Z \leq 42$, where the abundances decrease rapidly with increasing charge. The results presented here agree with those of our previous analyses where their data sets overlap. These previous analyses had been optimized for comparatively narrow charge regions. The data set used here has the advantage of a uniform data analysis procedure applied over the entire charge range and has more events in the $Z < 60$ charge region than previous analyses. Also, the normalization to iron derived here has a significantly smaller uncertainty.

II. EXPERIMENTAL TECHNIQUE

The third *High-Energy Astronomy Observatory* (*HEAO 3*) was launched 1979 September 20 into a circular orbit of altitude 495 km and inclination 43°.6. Data presented here were taken from 454 days prior to 1981 January 18. The Heavy Nuclei Experiment (HNE) on *HEAO 3* (illustrated schemati-

[1] Department of Physics and McDonnell Center for the Space Sciences, Washington University.
[2] California Institute of Technology.
[3] School of Physics and Astronomy, University of Minnesota.
[4] Now at Depauw University.
[5] Now at University of Chicago.

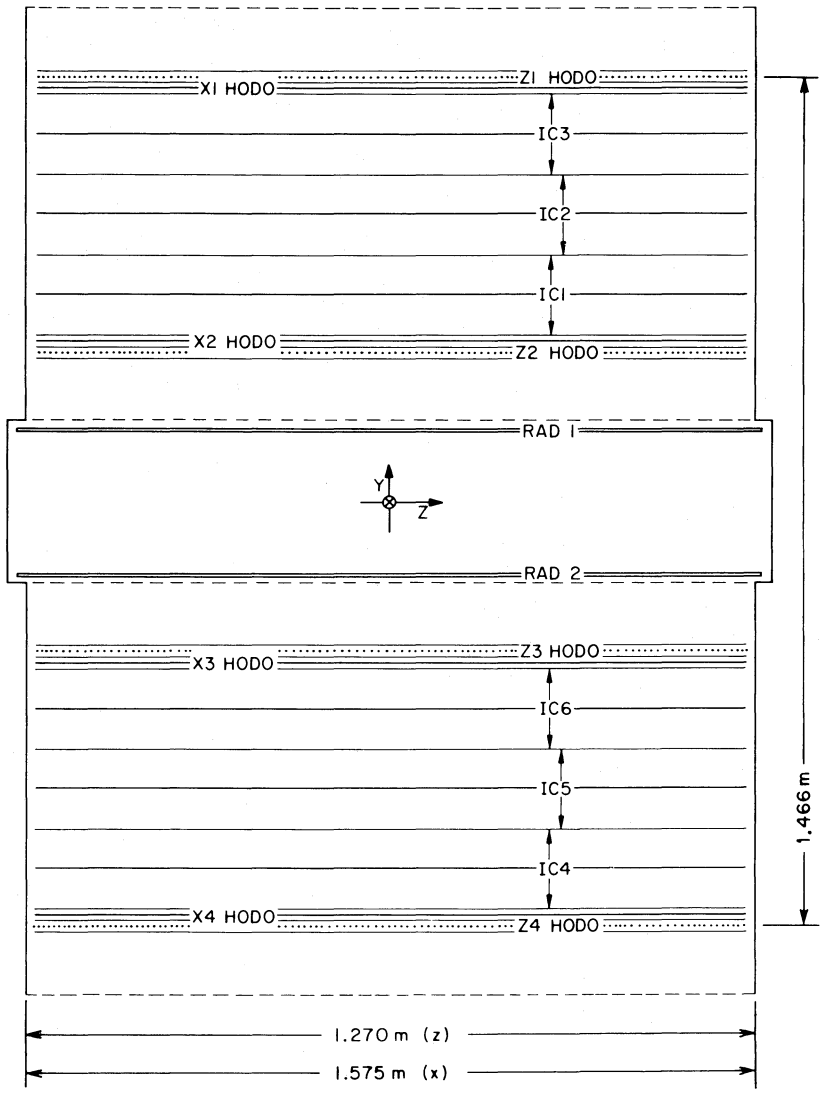

FIG. 1.—Schematic view of the HNE particle telescope. Diagram shows hodoscopes (labeled "HODO"), ion chambers (IC1 to IC6), and the dual radiator (RAD1 and RAD2) Cherenkov counter.

cally in Fig. 1) was composed of six ionization chambers, a Cherenkov counter with two Pilot 425 plastic radiators viewed by eight photomultiplier tubes, and four x–z pairs of multiwire ionization hodoscopes (Binns *et al.* 1981*b*). The ionization detectors were contained in two pressurized modules, each with three of the six ionization chambers and two of the four hodoscopes, with one module mounted on either side of the Cherenkov counter.

The charge determinations used here are based on the Cherenkov signal, i.e., the best estimate of Z for any one cosmic-ray particle is Z_C, given by 26 times the square root of the ratio of the Cherenkov signal of the particle to the Cherenkov signal of high-energy $_{26}$Fe nuclei. A selection on the ratio of the Cherenkov signal to the ionization chamber signal that effectively required that the particle had an energy greater than about 1.5 GeV nucleon^{-1} is used, so that the Cherenkov signal is greater than $\sim$90% of the nominal maximum signal for that Z (see Appendix).

The redundant charge measurements made on each particle are subjected to additional selection criteria (quality cuts) that reject events whose charge measurement has been impaired for some reason. Examples include nuclear interactions in the Cherenkov counter material, or generation of extra Cherenkov light in the glass windows of the photomultiplier tubes. These quality cuts substantially improve the resolution of the instrument and allow the measurement of relatively small abundances in the presence of a neighboring large abundance, e.g., the steep falloff over the interval $38 \leq Z \leq 42$. Careful studies of the distributions of the quality parameters as a function of charge confirm that the cuts are loose enough so that no significant charge biases are introduced. These selections are discussed in detail in Newport (1986). The most significant of these quality cuts are briefly described below:

1. *Charge changes between modules.*—We confine our analysis to cosmic-ray nuclei that penetrate at least one chamber in each of the two ion chamber modules, and we require that the signals in the two modules correspond to charges differing by no more than 10%. This requirement allows us to reject those events in which a nuclear interaction in the Cherenkov counter material changes the charge of the

particle. The observed distribution of fractional charge differences between modules has a roughly Gaussian core with a full width at half-maximum (FWHM) of ~8.5% due to statistical fluctuations in the signal, and a non-Gaussian tail due to nuclear interactions.

2. *Signal fluctuations within a module.*—If the particle traversed more than one of the three ion chambers within a module, then the signals from those chambers are required to agree with each other to within approximately 16% rms. The rms fluctuations in the square root of the signal (the charge) have a distribution which peaks at ~4.5%, and is at half-maximum at ~8%.

3. *Cherenkov agreement.*—In order to eliminate events with problems such as generation of extra Cherenkov light in the glass in the photomultiplier tubes, ratios of signals from opposing pairs of phototubes are required to agree with the average values of the ratio for all particles penetrating the Cherenkov detector at the same position. Particles with deviations larger than 14% (rms) are rejected. These rms deviations have a distribution with a peak at ~5.5% and a half-maximum value of 12%.

Since events which fail one test are most likely to fail several others (less than 10% failed only one test), and since the cuts mainly affect the non-Gaussian tails of the distributions, there is little sensitivity to the precise location of the cuts. The final data set, after all the quality cuts, contains 1585 events, with $Z_C > 32.5$.

A histogram of the Fe region of the measured charge spectrum is shown in Figure 2. The number of events is weighted for instrumental dead time and data processing selection effects, which are significant only for nuclei with $Z \lesssim 30$. The instrumental dead-time correction typically amounts to a factor of ~2 below $Z \sim 30$. Above that charge the dead-time correction is negligible, due to use of a high-Z priority system in the instrument. The data processing selection effect arises from the selection of a random sample of exactly 1/40 of the events with $Z < 30$ to produce a manageable data set. Neither factor introduces a significant statistical or systematic uncertainty. Since the energy cut, at about 1.5 GeV nucleon^{-1}, is low enough to include some particles with Cherenkov signals which are not at maximum, the distribution of particle energies leads to a distribution of Cherenkov signals. This distribution is seen in the width and asymmetry of the Fe peak, which obscures the much smaller peaks of $_{25}$Mn and $_{24}$Cr. In the analysis, we account for this distribution by calculating the expected response for each element based on a model for its energy spectrum, and by fitting the measured Z_C distribution with those calculated response functions, i.e., we deconvolve the measured response. The derivation of the fitting functions, and of the systematic uncertainties associated with the deconvolution procedure, is given in the Appendix. The dotted line indicates our fit to the abundances of the elements in the interval $20 \leq Z \leq 28$. The number of Fe events, determined from the fit of Figure 2, is 7.71×10^6, with a statistical uncertainty of 3%, and a possible systematic uncertainty of $\lesssim$2.5% due to uncertainties in the fitting function.

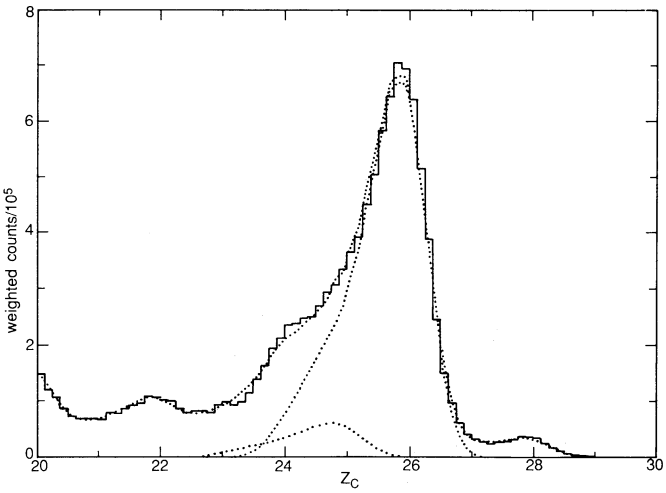

FIG. 2.—Charge histogram of particles in the Fe region; weighted counts are plotted as a function of Cherenkov signal in charge units. Dotted curve shows the fitted distribution calculated from a three-component Cherenkov model as described in the Appendix. Response functions for Fe and Mn are also shown. This fit is used to determine the $_{26}$Fe abundance.

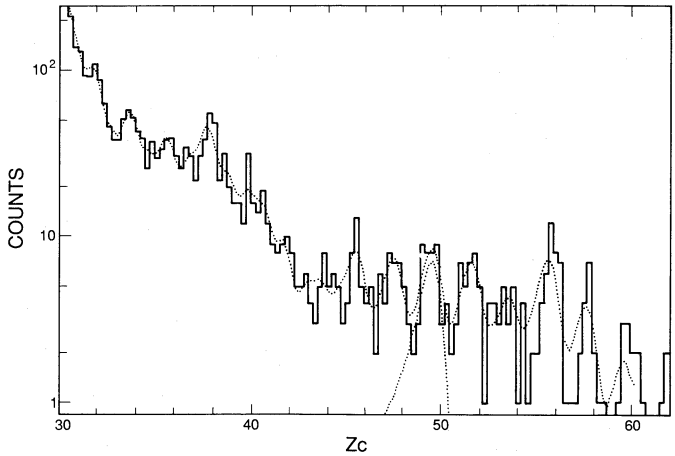

FIG. 3.—Charge histogram of particles in the $30 \leq Z_C \leq 62$ region. Dotted curve shows the results of fits with "pure" Cherenkov response functions as described in the Appendix. Response function for $Z = 50$ is also shown. Measured abundances are derived from these fits.

III. OBSERVATIONS

Figure 3 shows the charge histogram of the data for $30 \leq Z_C \leq 62$. Superposed are smooth dotted curves which show the results of fitting these histograms with the response functions, calculated as described in the Appendix. The resolution and statistical precision are such that abundance peaks of the even-Z elements are visible from 34 to 60. We do not report abundances for $29 \leq Z \leq 32$, because our resolution is inadequate to resolve those abundances in this data set. Similarly, elements with odd Z are not resolved, and the fit gives values for their abundance which are sensitive to the assumed fitting function, i.e., to the deconvolution procedure. Therefore, the abundances reported here are only for charge pairs, the abundance of each even charge being combined with that of the (generally less abundant) next lower odd charge immediately below it. The abundances are combined in this fashion since there is a residual tail extending to lower Z_C from each of the even charge peaks.

A small correction is made for interactions in the lids of the detector system, and for interactions in the material of the Cherenkov detector, as described by Newport (1986). For most elements, this interaction correction is small (<3%) because

the typical loss of ~15% due to fragmentation of the primary is offset by a similar gain of secondaries from interactions of heavier nuclei. For the Pt group, the Pb group, and the actinides, the offsetting gains are relatively small due to the lack of heavier nuclei, and the corrections amount to 8%, 15%, and ~15%, respectively. The corrected abundances are shown in Table 1.

In addition to the statistical uncertainties quoted in Table 1, there are systematic uncertainties arising in the deconvolution process, as described in the Appendix. Since the resolution is rather good, these uncertainties are generally small. The systematic uncertainties exceed the statistical uncertainties only for $Z = 33$ to 34, and for $Z = 41$ to 42, where the abundances are changing rapidly with Z and there are relatively large abundances of odd Z elements. For $Z = 41$ to 42, the systematic uncertainty is ~20%. For the entire charge region $33 \leq Z \leq 60$, the rms deviation of the abundances of all the odd-even pairs among various plausible fits is about 8%. The uncertainties for each charge pair are tabulated in Table 1.

In the $Z > 60$ charge region, the charge spectrum (Fig. 4) does not show the well-resolved peaks observed at lower charges. However, with a resolution no better than 0.34 charge units, and with fewer than five particles per unit charge interval, we cannot expect to see statistically significant peaks in this charge region. Since we cannot directly demonstrate that the relatively good resolution seen for $Z \leq 60$ continues at higher charges, and since there are relatively few events with $Z > 60$ in any case, we group these nuclei into just four charge intervals and simply count the number of events in each group. The groups are the "light secondaries" (LS), $61.5 \leq Z_C \leq 69.5$; the "heavy secondaries" (HS), $69.5 \leq Z_C \leq 73.5$; "Pt" (the Pt group), $73.5 \leq Z_C \leq 80.5$; and "Pb" (the Pb group), $80.5 \leq Z_C \leq 83.5$. Note that this data set has no events with $Z > 83$ (Bi); thus the Pb abundances may be compared to those quoted elsewhere for $Z = 81$ through 86.

IV. COMPARISONS

Abundances derived from the fits for $Z \leq 60$, and from counting for $Z > 60$, are reported in Table 1 and are compared there to our previously published abundances (Binns *et al.* 1983*b*, 1985; Stone *et al.* 1983). The agreement with our previous reports is generally good. In our preliminary results for $26 \leq Z \leq 42$ (Binns *et al.* 1981*a*, 1983*b*), we required better knowledge of the particle energy, and calculated the charge on the basis of both Cherenkov and ionization signals. In that data set, we had better resolution, but significantly less statistical precision. We do not report abundances here for the relatively abundant elements with $Z < 33$, where resolution is

TABLE 1

RELATIVE ABUNDANCES (Fe = 10^6)

Element	This Work	Sys	*Ariel*[a]	Previous[b]	UHGCR	Norm
32	...	...	...	91^{+12}_{-8}	91^{+12}_{-8}	
33–34	51.2 ± 3.7	6.0	66 ± 5	52 ± 6	61.1 ± 4.1	1.0
35–36	35.1 ± 3.0	1.0	39 ± 4	30 ± 8	36.6 ± 2.5	1.0
37–38	39.6 ± 3.1	2.7	36 ± 4	43 ± 6	37.8 ± 2.9	1.0
39–40	22.2 ± 2.6	1.2	24 ± 4	18 ± 5	22.8 ± 2.3	1.0
41–42	[15.4 ± 2.1]	2.5	17 ± 4	11 ± 3	11.0 ± 3.0	1.0
43–44	4.6 ± 1.2	0.3	3 ± 2	...	4.1 ± 1.1	1.0
45–46	6.7 ± 1.4	0.4	5 ± 2	...	6.2 ± 1.1	1.0
47–48	5.5 ± 1.3	0.3	5.5 ± 1.3	...	5.5 ± 0.9	1.0
49–50	6.3 ± 1.5	0.2	5.3 ± 1.0	5.7 ± 1.3	5.6 ± 0.8	1.0
51–52	5.2 ± 1.4	0.3	7.4 ± 1.0	3.0 ± 1.0	6.7 ± 0.8	1.0
53–54	3.1 ± 1.2	0.6	4.3 ± 1.1	3.5 ± 0.9	3.8 ± 0.8	1.0
55–56	6.3 ± 1.6	0.5	7.9 ± 1.2	6.2 ± 1.0	7.4 ± 1.0	1.0
57–58	3.5 ± 1.3	0.4	1.8 ± 1.0	2.8 ± 0.9	2.4 ± 0.8	1.0
59–60	1.5 ± 1.1	0.1	2.3 ± 0.8	...	2.0 ± 0.7	1.0
LS(62–69)	6.4 ± 0.9	...	7.3 ± 0.9	3.54 ± 0.63	6.9 ± 0.6	4.0
HS(70–73)	$2.0^{+0.7}_{-0.5}$	...	1.9 ± 0.5	$1.04^{+0.45}_{-0.33}$	1.9 ± 0.4	2.0
Pt(74–80)	5.1 ± 0.8	...	5.7 ± 0.8	4.38 ± 0.71	5.4 ± 0.6	3.8
Pb(81–83)	$1.2^{+0.6}_{-0.4}$	...	2.0 ± 0.6	$1.04^{+0.45}_{-0.33}$	1.6 ± 0.4	1.2
Actinide(88–100)	...	...	0.4 ± 0.2	$0.06^{+0.14}_{-0.05}$	$0.13^{+0.12}_{-0.05}$	1.6

NOTE.—Comparison of measured abundances corrected to top of detector for *HEAO* HNE and *Ariel*. An estimate of the systematic uncertainty due to the deconvolution procedure for HNE is in the column labeled "Sys" (see the Appendix). The previous HNE work tabulated here is based on data sets with resolution good enough that such errors are small; however, there are uncertainties in the normalization to Fe in the older works. The column labeled "UHGCR" is our best estimate for the abundances, combining results from our *HEAO* instrument, and from *Ariel*, as described in the text. The normalization factor for plotting Figs. 5, 6, and 8 ("Norm") is the sum of weight factors for each of the elements included in the abundance measurement. The weight factor is 0.8 for even-numbered elements, 0.2 for odd-numbered elements, 0 for $Z > 83$ except for 90 and 92.

[a] From Fowler *et al.* 1987.

[b] From the *HEAO* HNE (Binns *et al.* 1983*b*; Stone *et al.* 1983; Binns *et al.* 1985; Binns *et al.* 1982).

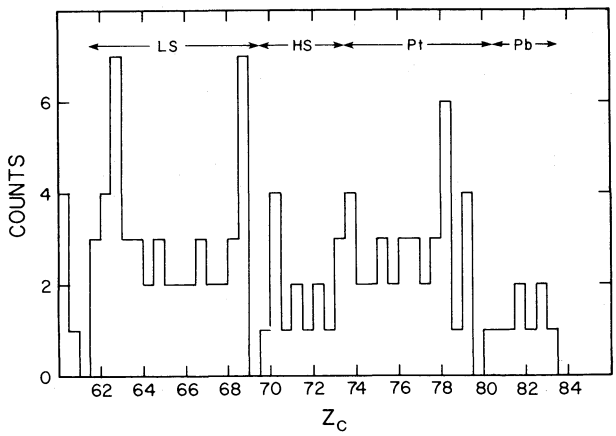

FIG. 4

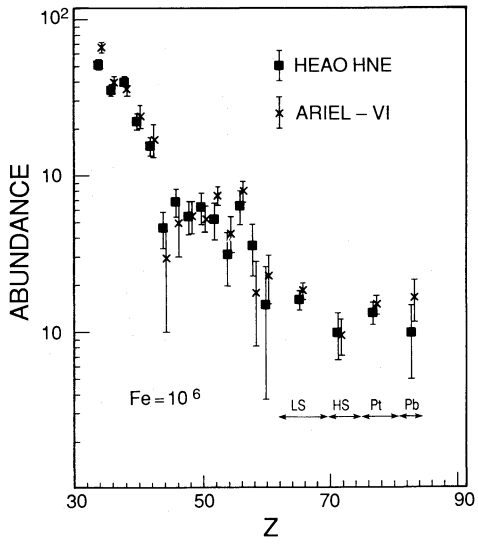

FIG. 5

FIG. 4.—Charge histogram for particles in the $Z > 60$ region. Charge ranges over which events are summed as indicated.

FIG. 5.—Comparison of relative abundances determined here with those from *Ariel 6* (Fowler *et al.* 1987). Abundances above $Z = 60$ are normalized to the widths of the charge bins. Unnormalized abundances and the normalization factors are in Table 1.

more important than statistics, because of the very large variations in abundance with charge. For the earlier $50 \leq Z \leq 58$ data set (Binns *et al.* 1983*a*; Stone *et al.* 1983), we required an energy above about 2.5 GeV nucleon^{-1}, but included events which were measured in either one or two ion chamber modules. That data set is comparable in both resolution and statistics to the one used here.

In our initial study of the Pt–Pb nuclei (Binns *et al.* 1985), only events with geomagnetic cutoff rigidity ≥ 5.0 GV (~ 1.5 GeV nucleon^{-1}) were analyzed, and only one ion chamber module was required. That data set was slightly larger, corresponding to 20% more Fe nuclei than this one. It did have significantly smaller LS and HS abundances (roughly a factor of 2; see Table 1). Since the present data set has a median rigidity of ~ 12 GV, and the earlier data set had a median rigidity of ~ 14 GV, the difference might indicate a substantial energy dependence of the HS and LS abundances. If the LS and HS elements have the same spectral softening observed for sub-Fe secondaries (Ormes and Protheroe 1983; Binns *et al.* 1988), then we would expect about 10% enhancement in the LS and HS to Fe ratios for the present data set relative to the earlier one, accounting for part of the difference between the two data sets. In the present data set, we observe a geomagnetic cutoff distribution for these HS and LS elements, which shows even more enhancement at low cutoffs than would be expected on this basis (i.e., a slightly softer spectrum than that of the sub-Fe secondaries), but which is statistically compatible with the spectrum of the sub-Fe secondaries. After allowing for the observed energy dependence, the remaining difference between the two measurements is most easily explained as a statistical fluctuation of roughly 1.8 standard deviations. We do not feel that our limited statistical precision justifies claiming a significant spectral difference between the Fe secondaries and the LS and HS elements.

It should be noted that in addition to variations in resolution and statistics, some uncertainty in the comparison between the previous and current data sets (and the following comparison to *Ariel 6* data) may arise from the fact that they have different energy distributions. We have no direct evidence that the energy spectra of the various primary species with $Z \geq 40$ are the same as that of Fe, nor that the spectra of the corresponding secondaries are the same as those of the sub-Fe secondaries. Certainly, the spectral shape of the secondaries is likely to differ from that of the primaries, as observed for the ligher elements (Binns *et al.* 1988). We do not have enough data to test these possibilities.

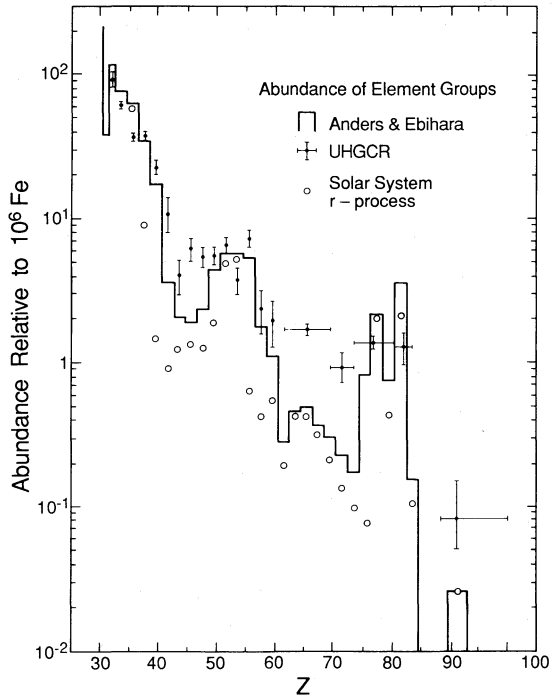

FIG. 6.—Comparison of the compilation of observed UHGCR abundances, determined here with the solar system (meteoritic) abundances compiled by Anders and Ebihara (1982). Abundances above $Z = 60$ are normalized to the width of the charge bins, using the factors from Table 1. Except for $Z = 31$ and $Z = 32$, the Anders and Ebihara histogram combines abundances for a pair of elements; each even-Z abundance is combined with the next lower odd-Z abundance. For the UHGCR abundances, the bin width is indicated by the horizontal line through the point. For reference, the r-process abundances from the decomposition of Binns *et al.* (1985) are indicated by the open circles for the same even-odd pairs.

In Figure 5, we compare the abundances reported here to the *Ariel 6* abundance measurements (Fowler *et al.* 1987). The agreement is strikingly good. In Figures 5 and 6, the abundances are normalized to compensate for the varying widths of the charge bins. These plotting normalization factors are sums of weight factors for each of the elements included in the abundance measurements. In order to allow for the even-odd effect, the weight factors are chosen to be 0.8 for even-numbered elements, and 0.2 for odd-numbered elements. This normalization has no effect on an even-odd pair and is correct for other bins if the odd/even ratio is 0.25. The normalization factors and the unnormalized abundances are given in Table 1.

Since the various *HEAO* and *Ariel* data sets are in such good agreement, it is useful to combine the data, reducing the statistical uncertainties. In combining the data, we use the weighted average of our current abundances, reported here, with those of *Ariel 6* (Fowler *et al.* 1987) for most elements. For $Z = 32$ and for the $Z = 41$, 42 pair, we feel that the earlier *HEAO* measurement (Binns *et al.* 1981*a*, 1983*b*) (with better resolution than either the present *HEAO* data set or *Ariel 6*) should be used. For the "actinides" ($88 \leq Z \leq 100$), we have scaled our previously reported actinide/Pt-Pb ratio (Binns *et al.* 1982) with the currently reported Pt-Pb/Fe ratio to derive an actinide/Fe ratio (reported as "previous" in Table 1). That ratio is averaged with that of *Ariel 6*. The current *Ariel 6* value for the actinide/Pt-Pb ratio is larger than ours, but statistically compatible. The resultant data set, covering the Z range from 32 to 100, is our best estimate for the observed abundances of near-Earth ultraheavy galactic cosmic rays (UHGCRs), and is shown in Table 1.

These UHGCR abundances (normalized for plotting) are shown in Figure 6 as a function of charge and are compared with the Anders and Ebihara (1982) compilation of solar system abundances. (The new compilation of Anders and Grevesse 1989 differs by amounts which are not significant, compared to our statistical precision.) The general trend of the two compilations is similar. The most obvious difference is that many elements which are rare in the solar system are more abundant in the cosmic rays, as expected from the production of secondaries by nuclear interactions (mainly spallation) in the interstellar medium. We have calculated the effect of these interactions by the methods of Brewster (1984) and Brewster, Freier, and Waddington (1983, 1985). Other differences seem to arise from a fractionation (Meyer 1985; Israel 1986) of the cosmic-ray source material before acceleration, by a process which is strongly correlated with first ionization potential (FIP).

To understand the implications of these observed abundances, we compare them with those expected from models based on various source abundances, after allowing for fractionation and propagation through the Galaxy. We will consider three standards for the cosmic-ray abundances, in which the source composition is either (i) similar to the solar system, (ii) similar to the *s*-process derived from solar system abundances, or (iii) similar to the *r*-process derived from solar system abundances.

Both *s*-process and *r*-process abundances are sensitive to the physical characteristics of the site of nucleosynthesis, such as temperature and neutron fluence. Only for solar system matter are the resulting abundances sufficiently well-studied to provide a basis for a decomposition into *s*- and *r*-process abundances. Thus, the solar system *s*- and *r*-process abundances are presumably only one representation of a continuum of possible abundance spectra. We will use the decomposition of Binns *et al.* (1985), which is based on the solar system abundances of Anders and Ebihara (1982). The *r*-process abundances are shown for reference in Figure 6, along with the solar system abundances.

For each of these alternatives, we also consider the effect of modifying the source abundances by a multiplicative FIP fractionation factor, f, which is a sloping step function (Letaw *et al.* 1984) of first ionization potential (step FIP),

$$f = \begin{cases} 1 & (\mathrm{FIP} < 7\ \mathrm{eV}), \\ \exp\left[-0.27\ (\mathrm{FIP} - 7)\right] & (7 \leq \mathrm{FIP} \leq 13.6\ \mathrm{eV}), \\ 0.168 & (\mathrm{FIP} > 13.6\ \mathrm{eV}). \end{cases}$$

This function was derived from an analysis of abundances of elements with $Z \leq 28$. In previous UH studies (Binns *et al.* 1981*a*, 1983*b*; Newport 1986), this function has provided better fits than an exponential function of FIP. We use the standard leaky box model for propagation (as formulated in Brewster 1984; Brewster *et al.* 1983, 1985) and concentrate on the results of invoking different types of cosmic-ray source material to explain the observed abundances. This "standard" model includes the commonly used rigidity-dependent path length distribution of Ormes and Protheroe (1983):

$$\lambda(\mathrm{g\ cm^{-2}}) = \begin{cases} (26.9)[1 + (1.88/R)^2]^{-3/2} R^{-0.7} & (R < 11.4\ \mathrm{GV}); \\ (25.8) R^{-0.7} & (R \geq 11.4\ \mathrm{GV}). \end{cases}$$

The propagation uses the semiempirical fragmentation cross sections of Silberberg and Tsao (1973*a*,*b*) which are calculated at 2.3 GeV nucleon^{-1} and assumed to be independent of energy. Propagated abundances are summed, as necessary, for comparison to the UHGCR observations.

We consider a variety of source models based on the standards listed above, and develop a "best" *s*-process and *r*-process mixture model which is consistent with our observations. These various models are summarized in Table 2 and Figure 7; the details of the models and the progression follow.

In Figure 7*a*, we show the ratio of the UHGCR abundances to the propagated abundances for an unfractionated solar system source (Anders and Ebihara 1982), corresponding to model 1 of Table 2. As expected from the preceding discussion, the trend of the data is generally the same as the calculation, but there are deviations of roughly a factor of 2. The error bars indicated in Figure 7*a* (and the succeeding figures) are uncertainties of the UHGCR abundances only. There could be significant additional uncertainties which are difficult to evaluate. These include uncertainties in the nuclear interaction cross sections used in the propagation calculation, uncertainties in the solar system source abundances, and, possibly, charge dependence of the energy spectra. We calculate a goodness of fit parameter, χ^2, between the UHGCR abundances and the model abundances. However, since only the statistical measurement uncertainties in the UHGCR abundances are included, the reduced χ^2_ν values obtained are typically much larger than 1. They do provide qualitative discrimination between various source models, even though they cannot be used to determine a probability for the model. The reduced χ^2_ν values are given in Table 2 for each of the models discussed here.

Figure 7*b* shows the results of using the same propagation technique on the same source material, modified by step FIP fractionation (model 2 of Table 2). The agreement between the

TABLE 2

FITS OF MODELS TO OBSERVED UHGCR ABUNDANCES

Model	K_s	K_r	K_s/K_r	G&M	FIP	Z Range	χ^2_ν	ν	Comment
1.....	$\equiv 1$		$\equiv 1$	No	No	32–100	20.6	20	Comparison to propagated A&E solar system, see Fig. 7*a*
2.....	$\equiv 1$		$\equiv 1$	No	Step	32–100	4.87	20	As above, but with FIP fractionation, see Fig. 7*b*
3.....	1.002 ± 0.03		$\equiv 1$	No	Step	32–100	5.13	19	As above, but allowing the Fe normalization to vary
4.....	0.96 ± 0.03		$\equiv 1$	No	Step	32–60	3.12	14	As above, but with restricted Z range
5.....	1.07 ± 0.03		$\equiv 1$	Yes	Step	32–100	4.17	19	Using the G&M correction, compare to Fig. 7*c*
6.....	1.02 ± 0.03		$\equiv 1$	Yes	Step	32–60	1.94	14	Restricted Z range, see again Fig. 7*c*
7.....	0.91 ± 0.07	1.19 ± 0.07	0.76 ± 0.17	Yes	Step	35–60	2.32	11	With separate K_s and K_r
8.....	$0.26^{+0.45}_{-0.26}$	26.4 ± 0.48	$0.10^{+0.15}_{-0.10}$	Yes	Step	62–100	0.15	3	Best fit for $Z > 60$
9.....	0.59 ± 0.47	2.32 ± 0.49	0.25 ± 0.25	Yes	No	62–100	1.95	3	Not unreasonable alternative fits for $Z > 60$
10.....	1.76 ± 0.012		$\equiv 1$	Yes	No	62–100	2.14	4	
11.....	1.82 ± 0.12		$\equiv 1$	Yes	Step	62–100	2.45	4	
12.....	Best Source (see Table 3)				Step	32–100	1.31	20	See Fig. 7*d*

NOTE.—Parameters of fits to the propagated abundances for models of the cosmic-ray source material given by $K_s s_i + K_r r_i$, where r_i and s_i represent the r- and s-process components of the solar system abundances. The solar system is, by definition, given by $K_s = K_r = K = 1$. The column headed "G&M" indicates the (Grevesse and Meyer 1985) correction to Pb and Ge. Reduced χ^2_ν is specified; degrees of freedom are given by ν.

calculated and the measured abundances is much improved, confirming the observation from the abundances of elements with lower Z that FIP organizes the ratio of cosmic-ray abundances to solar system abundances. This improvement is also seen in the reduction of χ^2_ν from 20.6 to 4.9. The UHGCR abundances agree with the solar system source with step FIP to within $\pm 35\%$ from charge 32 to 60 with the most significant difference occurring at $_{32}$Ge, but agree less well for $Z > 60$, with the "Pb" abundance substantially low, and the "Pt," "HS," "LS," and "actinide" abundances substantially high.

If we try to improve the agreement by allowing the normalization to iron to vary as a free parameter (K), then the best-fit value of K is 0.2% larger than that of the solar system (model 3 of Table 2), a negligible difference. The decrease in χ^2 is much smaller than the decrease in the number of degrees of freedom, thus the reduced χ^2_ν increases. Considering only the restricted charge range, $32 \leq Z \leq 60$, the best fit K is 4% smaller than the solar system (model 4 of Table 2), still a negligible improvement.

One possible explanation for the relatively low abundance of $_{82}$Pb, and also for $_{32}$Ge, would be a volatility related fractionation process instead of FIP fractionation (Binns *et al.* 1985). Apart from these two elements, FIP and volatility are closely correlated, and we cannot distinguish between fractionation models based on either. Alternatively, Grevesse and Meyer (1985) have reexamined spectroscopic data on photospheric abundances and have suggested that the photospheric abundance of Pb (and Ge) is about 0.63 (0.61 for Ge) of the standard meteoritic abundance (Anders and Ebihara 1982). Thus, the UHGCR Pb and Ge abundances would be in agreement with that of the solar photosphere, but different from the meteoritic abundances. In Figure 7*c* and in models 5 and 6 of Table 2, we show a comparison of UHGCR abundances with propagated solar system abundances, modified accordingly, with FIP fractionation. As expected, the fit is much improved for the two modified elements, Pb and Ge. An explanation proposed by Margolis and Blake (1985) for a low Pb abundance is a source with incomplete s-process recycling due to limited neutron flux. This explanation does not address the Ge abundance.

However, none of these explanations for low Pb abundance are relevant to the overabundance of Pt and its secondary elements relative to Fe. It is likely that the secondary abundances are high just because the abundance of the Pt group primaries which produce them is high. The Pt group is generally considered to be an indicator of r-process nucleosynthesis (see Fig. 6), so we have calculated model abundances for an r-process source. The r- and s-process source abundances are taken from the decomposition of Binns *et al.* (1985), modified by subtracting the Grevesse and Meyer correction from the r-process component of the Pb, and are represented by r_i and s_i, the r- and s-process abundances of the element i relative to Fe. Fractionation and propagation were modeled as described earlier, i.e., sloping step function FIP fractionation and propagation according to Brewster *et al.* (1983, 1985). A pure r-process source does organize the $Z > 60$ abundances much better than a solar system source. However, the charge region below 60 is in poor agreement with an r-process source, with the observed values of s-process elements such as $_{38}$Sr, $_{40}$Zr, and $_{56}$Ba having large overabundances. The UHGCRs in the $Z > 60$ charge region are roughly 3 times more abundant than calculated for a solar system r-process source (relative to observed Fe), as detailed in the next paragraph. This enhancement is due primarily to the Pt group abundances; the actinide enhancement has marginal statistical significance, and the source abundances of the largely secondary elements with $62 \leq Z \leq 74$ are not well determined.

We can use a two-parameter fit to determine quantitatively how large an enhancement of r-process source material is present in the $Z > 60$ abundances. Thus, we fit the abundance ratios with the expression $K_s s_i + K_r r_i$ where K_s and K_r specify

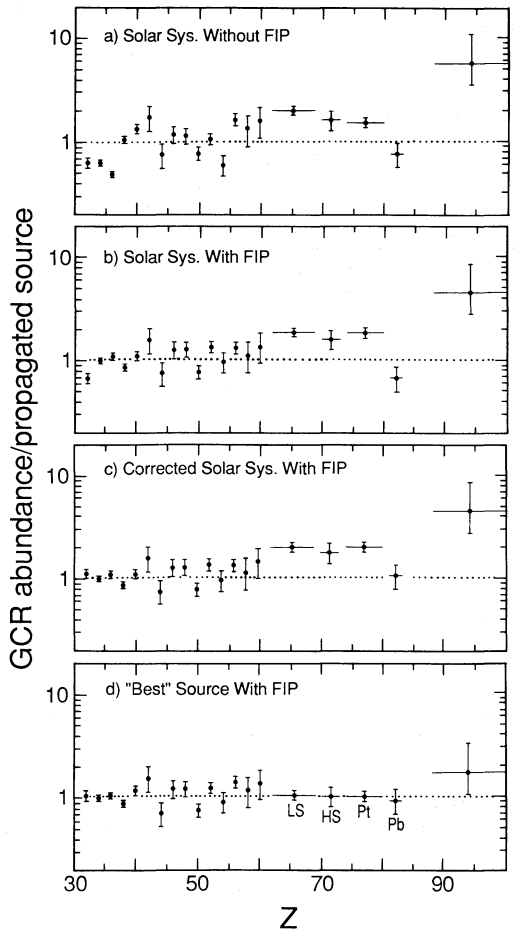

FIG. 7.—(*a*) Comparison of the UHGCR abundances with propagated Anders and Ebihara (1982) source material. No FIP correction is made (see text). Comparison is shown by plotting the ratio of the measured UHGCR abundances to the calculated abundance vs. atomic number Z. (*b*) Ratios of UHGCR abundances to calculated abundances vs. Z with propagation and fractionation (step FIP) of a solar system cosmic-ray source material as described in the text. (*c*) Ratios vs. Z with the source composition modified to reflect the Grevesse and Meyer (1985) correction to the Pb and Ge abundances, as described in the text. (*d*) Ratios vs. Z with the "best source" composition described in the text and shown in Table 3.

the separate normalizations of the *s*- and *r*-process components, and $K_s = K_r = 1$, by definition, for the solar system abundances. If we interpret the $Z > 60$ abundances relative to Fe in this fashion as a mixture of *r*-process and *s*-process components fractionated by step FIP, then the best-fit s/r ratio (K_s/K_r) is 0.10 that of the solar system, with an upper limit (84% confidence level) of 0.25, and a lower limit of 0. (See model 8 of Table 2.)

We have also compared three other models with the $Z > 60$ abundances (models 9, 10, and 11 in Table 2). The fits to these models, while clearly not as good as for model 8, do have tolerably small values of reduced χ^2_ν. All of these fits have K_r substantially larger than one, i.e., they all have enhanced *r*-process components. They include enhanced *r*-process without FIP fractionation (model 9), and enhanced solar system (with Grevesse and Meyer correction) with or without FIP fractionation (models 10 and 11), where enhanced solar system indicates $K_s = K_r = K > 1$. Models without the Grevesse and Meyer correction to the Pb and models with $K_r \sim 1$ give much larger reduced χ^2_ν ($\sim$4–10 and larger) than the listed models.

All of these source composition models (8–11) have substantially enhanced Pt abundances. With enhanced Pt primaries, the secondary (LS, HS) abundances predicted by the simple standard leaky box model are consistent with the observations. No more elaborate model is justified, especially in view of the limited statistics and the uncertainties in the cross sections (Waddington *et al.* 1987*a*, *b*).

We can also examine the UHGCR abundances of elements with $Z \leq 60$ for *r*-process enhancements in the source composition, but expect little enhancement, since the solar system source model fits this charge range well. If we consider the abundances for $Z \leq 60$ only (but excluding $Z = 32$, 33, and 34 abundances, because in the solar system they have contributions from other nucleosynthetic processes) and interpret them as a mixture of *r*- and *s*-process components fractionated by step FIP (model 7 of Table 2), then the best-fit s/r ratio is 0.76 ± 0.17 times that of the solar system, similar to the value reported by Stone *et al.* (1983), and K_r is 1.19 ± 0.07, not much larger than 1. In contrast, for $Z > 60$ (model 8) the data show a distinct *r*-process enhancement with an s/r ratio of $0.10^{+0.15}_{-0.10}$ and a K_r of 2.64 ± 0.48.

V. DISCUSSION AND CONCLUSIONS

The elements in the range $33 \leq Z \leq 60$ are well fit by the model which assumes a solar system source with step FIP fractionation; over the charge range $35 \leq Z \leq 60$ where the decomposition into *r*- and *s*-process components (Binns *et al.* 1985) is meaningful, the best-fit mixture of *s*- and *r*-process components show a slight enhancement of *r*-process compared to the solar system mixture. Pt and its secondaries (the HS and LS groups) are best fitted by a predominantly *r*-process source with step FIP; the Pb and Ge abundances resemble those in the photosphere (Grevesse and Meyer 1985), rather than in meteorites. We have, therefore, compiled in Table 3 a best mixture model (model 12 of Table 2) for the source composition with all these features: for $Z = 32$, the source abundance is given by Grevesse and Meyer (1985); for $Z = 33$, 34, the source abundance is given by Anders and Ebihara; for $35 \leq Z \leq 60$, the source abundances are given by $0.91s_i + 1.19r_i$, where r_i and s_i are based on our decomposition of the Anders and Ebihara (1982) solar system (Binns *et al.* 1985); for $62 \leq Z \leq 100$, the "best" source abundances are given by $0.26s_i + 2.64r_i$, where our *r*-process abundances have been corrected per Grevesse and Meyer. These best mixture source abundances are compared to the Anders and Ebihara solar system abundances in Figure 8.

Although the evidence for an *r*-process enhancement in the Pt group is compelling (note the fit values of $K_r \sim 2$ for the range $Z > 60$ in all of models 8–11), such is not the case for the apparent *s*-process depletion. Best-fit values of K_s range from 0.26 (with a statistical lower limit of 0.00) to 1.82. Pb is the only abundant element in this charge region expected to have a significant *s*-process component. The solar system and *s*-process abundances of Pb are not particularly well known. We have already commented on the differences between meteoritic Pb abundances and photospheric Pb abundances. In addition, meteoritic Pb abundances are not consistent among the different compilations of meteoritic abundances (see, for example, Cameron 1973; Cameron 1982*a*; Anders and Ebihara 1982; Anders and Grevesse 1989). The decomposition into *r*- and *s*-process components introduces still further uncertainty, especially for Pb, which is an endpoint of the *s*-process (e.g., Margolis and Blake 1985). Cameron's (1982*b*) decomposition, for

TABLE 3

COMPILATION OF "BEST" SOURCE ABUNDANCES

Z	UHGCR	Best Source Unfrac	Best Source Frac	Comment
32	91 + 12, −8	80.0	79.4	G&M 1985
33	61.1 ± 4.1	7.54	4.47	A&E 1982
34		69.0	41.6	
35	36.6 ± 2.5	14.7	5.07	
36		57.8	12.3	
37	37.8 ± 2.9	9.14	11.6	
38		24.7	31.2	
39	22.8 ± 2.3	4.74	6.00	
40		11.2	14.1	
41	11 ± 3	0.72	0.91	
42		3.00	2.34	
43	4.1 ± 1.1	0.0	0.0	
44		2.27	2.60	
45	6.2 ± 1.1	0.44	0.49	Best-fit r, s mix:
46		1.70	1.49	$K_s = 0.91$,
47	5.5 ± 0.9	0.66	0.71	$K_r = 1.19$
48		1.85	1.36	$35 \leq z \leq 60$
49	5.6 ± 0.8	0.23	0.29	
50		4.38	5.06	
51	6.7 ± 0.8	0.44	0.36	
52		6.23	4.58	
53	3.8 ± 0.8	1.18	0.59	
54		5.56	1.76	
55	7.4 ± 1.0	0.48	0.61	
56		4.49	5.68	
57	2.4 ± 0.8	0.49	0.61	
58		1.25	1.58	
59	2.0 ± 0.7	0.20	0.26	
60		0.97	1.23	
62	6.9 ± 0.6	0.55	0.70	
63		0.27	0.34	
64		0.83	1.06	
65		0.16	0.20	
66		0.95	1.21	
67		0.24	0.30	
68		0.60	0.76	
69		0.09	0.12	
70	1.9 ± 0.4	0.49	0.62	
71		0.09	0.12	
72		0.29	0.37	Best-fit r, s mix:
73		0.04	0.05	$K_s = 0.26$,
74	5.4 ± 0.6	0.24	0.23	$K_r = 2.64$
75		0.14	0.14	$62 \leq z \leq 100$
76		1.93	1.54	
77		1.90	1.36	
78		3.82	2.82	
79		0.52	0.36	
80		0.67	0.34	
81	1.6 ± 0.4	0.23	0.29	
82		2.36	2.66	
83		0.34	0.40	
90	$0.13^{+0.12}_{-0.05}$	0.09	0.11	
92		0.02	0.03	

NOTE.—Abundances relative to 10^6 Fe. UHGCR abundances are repeated from Table 1 to indicate uncertainties in source abundances; read the discussion of uncertainties in the text. Source abundances less than 1 are highly uncertain. The abundance for a group of elements is relatively well determined; within a group, the relative abundances are derived from those of the solar system (Anders and Ebihara 1982). Column labeled "Unfrac" is the "best" mixture abundance before fractionation. The "Frac" column has been adjusted by the FIP fractionation function f (see § IV of the text) and renormalized so that Fe is still 10^6.

instance, attributes essentially all the Pb to the *s*-process. In that case, the observed UHGCR source abundances would correspond to a $K_s \sim 0.8$, implying little or no depletion of *s*-process. Thus, it is not possible to determine the degree of depletion of the *s*-process in the UHGCR source abundances relative to the solar system abundances, because of the uncertainty in the solar system Pb abundance and the uncertainty in the *s*-process contribution to that abundance. On the other hand, the solar system abundance of the Pt group is better determined and is primarily the result of an *r*-process. Thus, the relatively large Pt abundance in the UHGCR, in the absence of a corresponding Pb enhancement, is a direct indication of an *r*-process enhancement in the UHGCR source in this charge region.

The uncertainties in the solar system Pb abundance appear to be small enough to exclude the possibility that the UHGCR Pb abundance is enhanced above those in the solar system. The smallest solar system Pb abundance quoted in the references listed above is the photospheric abundance of Grevesse and Meyer (1985), or Anders and Grevesse (1989). This photospheric abundance has a rather small quoted uncertainty (12%) and is the solar system abundance used in the comparison shown in Figure 7*c*. Any of the other (larger) solar system abundances would imply a relative depletion of Pb in the UHGCR.

In Figure 7*d*, we show a comparison of UHGCR abundances with those given by our best source (model 12 of Table 2), after FIP fractionation and propagation. Table 3 shows these best source abundances both before and after FIP fractionation. The abundances, before fractionation, are indicative of the nucleosynthesis history of the ultraheavies. The fractionated abundances presumably result from the ionization state of the injected material, or of the source of the injected material; similar fractionation is observed in the solar corona (Breneman and Stone 1985). Estimation of uncertainties is quite difficult. Elements which have similar abundances in the UHGCR and in the best source should be predominantly primary in the cosmic radiation, and, hence, the uncertainties in the source should be comparable to those in the UHGCRs. Source abundances of those elements whose cosmic-ray abundances are dominated by secondary production (generally those with abundances less than 1 per 10^6 Fe) are highly uncertain. Further uncertainties are introduced by the limited sample size and resolution, which require us to analyze element pairs and groups rather than individual elements.

The predominantly secondary abundances in the

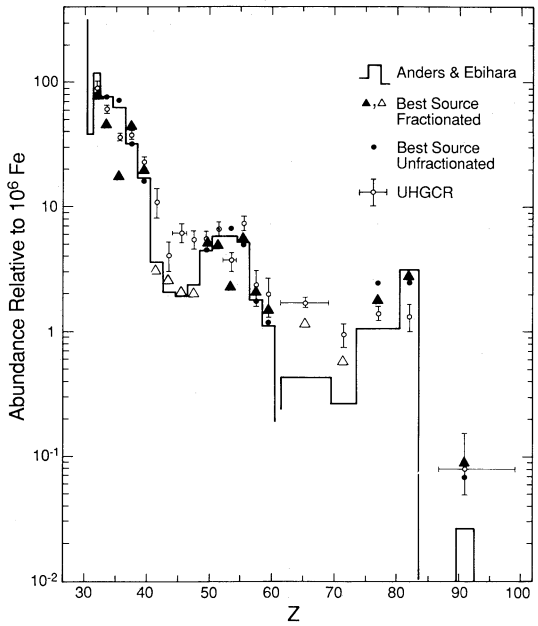

FIG. 8.—Comparison of the "best" source mixture composition with the solar system (meteoritic) abundances compiled by Anders and Ebihara (1982), and the observed UHGCR abundances presented here. Abundances of charge groups are presented in accordance with the UHGCR observations, and are normalized as in Figs. 5 and 6. Use of open triangles for the predominantly secondary elements is intended to emphasize the uncertainty in these source abundances—see text.

$40 \leq Z \leq 49$ interval are well fitted by the standard propagation model used here (Brewster 1984; Brewster, Freier, and Waddington 1983, 1985), without invoking truncation of path lengths (Klarmann *et al.* 1983; Margolis 1983), continuous acceleration (Silberberg *et al.* 1983), or other elaborations. If we assume enhanced *r*-process source abundances to explain the overabundance of the Pt relative to the solar system, then the abundances of the HS and LS groups can also be explained without any elaborations on the standard propagation model.

The *r*-process enhancement above $Z = 60$ might indicate the admixture of some "unusual" heavy ($Z > 60$) *r*-process material in a medium which is otherwise roughly similar to the solar system in composition. This *r*-process admixture is unusual only in the sense that its ratio of $Z > 60$ to $Z < 60$ abundances is not the same as in the solar system. It is not difficult to model an *r*-process which synthesizes only nuclei with $Z > 60$ (Schramm 1982). A calculated *r*-process abundance spectrum depends on such parameters as neutron bombardment flux and exposure time, just as the *s*-process spectrum does. Adjustment of these parameters allows modification of the spectrum; in particular, the regions separated by "magic" numbers of protons or neutrons (such as neutron number $N = 82$) can be enhanced or suppressed relative to each other. It is possible for some of the heaviest elements to fission, producing elements with $Z < 60$. The small observed enhancement for $Z < 60$ ($K_r = 1.19 \pm 0.07$) constrains the abundances of these fissioning elements. These observed *r*-process enhancements place some limits on physical conditions in the region where cosmic-ray nuclei are synthesized and represent evidence that these conditions differ from those in the region where the solar system material was produced.

We have presented here a coherent set of observations of abundances of ultraheavy galactic cosmic rays, from which we can derive abundances in the cosmic-ray source material. From these results, we conclude that although the galactic cosmic-ray source composition is qualitatively similar to that of the solar system, there are quantitative differences indicative of a different nucleosynthetic history for material in the cosmic-ray source regions of the Galaxy. Further theoretical study of the conditions leading to the source abundances reported here should contribute to a better understanding of the origins of cosmic rays.

This research was supported in part by NASA under grants NAG 8–498, 500, and 502; and NGR 05–002–160, 24–005–050, and 26–008–001. Brownlee Gauld's assistance in computer programming was exceptional.

APPENDIX

DECONVOLUTION PROCEDURE

Deconvolution of the charge abundances from the Z_C histogram requires knowledge of the instrument response function. At Fe, this response is dominated by the Gaussian smearing of the light signal in the Cherenkov system due to photoelectron statistics. The large abundance of Fe compared to neighboring elements and the relatively good statistical precision of the Fe data allow a useful comparison of the measured and calculated response functions, as shown in Figure 2. In order to calculate the response for higher charges, we must extend the calculation into regions where we have no calibration data and relatively poor statistical precision. This calculation is based on a specification of the rigidity (hence, energy or velocity) spectrum of each element, the light signal generated by a particle of given charge and velocity, and instrumental response factors such as photoelectron statistics. Newport (1986) has described in detail the calculation of the Fe response function, and we will only outline it briefly here, concentrating on some minor improvements we have made.

For Fe, where statistical precision is not a problem, the observed spectrum of geomagnetic cutoffs can be used to derive the rigidity (or energy) spectrum of the observed particles. The geomagnetic Störmer cutoff rigidity is calculated for each particle event, based on the location of the satellite at the time of the event, and on the direction of motion of the particle. Since the instrument is double-ended, there is an ambiguity of 180° in the direction of motion of most particles. For some particles ($\sim 15\%$), one of the two possible directions is clearly shadowed by the Earth, resolving the ambiguity. For the others, it is necessary to calculate two cutoff rigidities; these events are divided between the two cutoff rigidities in the spectrum, according to the probabilities calculated on the basis of an assumed local interplanetary spectrum. Newport used the Webber (1983) compilation of Fe spectra, measured near Earth, to calculate these probabilities; we have adjusted that spectrum slightly, to allow for the level of solar modulation appropriate to our 1979–1980 flight epoch. For our limited purposes, we used a force field model for solar modulation (Gleeson and Axford 1968) and applied the model as if the Webber spectrum was the interstellar spectrum. Thus, our values of the force field parameter, Φ, are relative and somewhat low. Since we are not very sensitive to this parameter, the limited sophistication of this model is not a

problem. For the same reason, this procedure cannot determine a reliable value of Φ, and the quoted values should not be used for other purposes. Adjustments in the level of the solar modulation affect the calculated width of the $_{26}$Fe peak and, hence, affect the $_{25}$Mn abundance derived from the fit. The observation that the Mn abundance is between 5% and 10% of the Fe abundance (Engelmann *et al.* 1983) limits the systematic uncertainty in the Fe abundance to ±2.5%. The adopted model has a Mn abundance of ~7.5% relative to Fe, with a Φ of 0.45 GV. Note that the rigidity spectrum observed by HNE with the data selections specified here is quite different from the local interplanetary spectrum, because the HNE observes events above a geomagnetic cutoff which constantly varies as the *HEAO 3* spacecraft spins and moves in its orbit. Newport assumed that all elements have the same spectral shape; we assume that each element is a mixture of primary and secondary components, with the spectral shape of the primary component being the same as that of Fe, and the spectral shape of the secondary component given by dividing the observed Fe spectrum by $E^{0.3}$ (where E is kinetic energy) (Binns *et al.* 1988).

Given the energy spectrum of a particular element, the mean light signal in the Cherenkov system is calculated as a function of energy. This light signal is assumed to have three components: Cherenkov light generated by the heavy nucleus, Cherenkov light generated by knock-on electrons (i.e., secondary electrons or delta rays), and scintillation light. Both the scintillation component and the Cherenkov component depend on the inverse square of the velocity ($1/\beta^2$), and hence, at high energies, can be combined into a single component with the velocity dependence of Cherenkov light, but with an altered index of refraction (i.e., an effective index). The velocity dependence of the knock-on component is given by Lezniak (1976) and rises with energy even at high energies, so that the light signal does not have the same asymptotic trend to a maximum as $\beta \rightarrow 1$ as does a "pure" Cherenkov signal. After the most probable light signal is calculated for a particular charge and energy, the signals are spread in a Gaussian fashion about that most probable value. They are then convolved with the assumed energy spectrum. The spreading is due to photoelectron statistics and has a standard deviation of 0.34 charge units for any element.

Since the spread of the light signal due to energy variations and velocity dependence grows with Z^2, while the Gaussian photoelectron spreading grows only with Z, the calculated response function at, for example, $Z = 50$ is noticeably different in shape from that of $_{26}$Fe. Figure 9 shows a fit to the charge region $40 \leq Z \leq 60$, based on a fitting function calculated as described above, and the fitting function for $Z = 50$.

Clearly, the data have a better peak to valley ratio than this fit. Therefore, Newport (1986) and Stone *et al.* (1987) made fits based on a purely Gaussian response function, which reproduces the good peak to valley ratio observed in the data. For the present paper, we have rejected the pure Gaussian, since we cannot construct a plausible model which does not have at least some non-Gaussian tail on the lower Z_C side of the peak. The main effect of adding or omitting these tails in the fit is to exchange odd-element abundances with abundances of the even element just above. Since we are only reporting abundances for sums of such pairs, our quoted abundances are not very sensitive to fitting functions. We have, however, considered a variety of changes to the response model, in order to establish the size of the systematic uncertainties which might be caused by using inappropriate fitting functions. The details of these models are specified below. Figure 10 summarizes the derived systematic uncertainties.

We have been unable to create any plausible models which involve variations of the energy spectrum. In order to produce peak to valley ratios as good as those seen in the data, it would be necessary to invoke drastic changes in the energy spectra, much larger than the solar modulation correction mentioned above. Similarly, we can find no plausible instrumental effect which would sharpen these peaks. The HNE makes a large number of charge measurements with its six ion chambers and eight phototubes. Consistency among these 14 measurements creates considerable confidence in the charge measurements.

It is possible that the assumed Cherenkov response of the HNE instrument as a function of velocity may be inaccurate for high velocities at high Z. At lower energies ($\lesssim$1.2 GeV nucleon^{-1}), we have not observed any large deviations from the model in our Bevalac Cherenkov calibration data (Garrard *et al.* 1983; Newport 1986; Klarmann *et al.* 1987), but all of the *HEAO* HNE measurements reported here were made at energies above the highest energy available for our calibrations. In particular, the energy dependence of the knock-on component of the light signal tends to spread out the response function. Because this component depends so strongly on the configuration of the instrument, we have used a model in which this knock-on component is omitted, and the Cherenkov signal is renormalized to compensate for the missing ~6% knock-on contribution. In this simple 'one-component' model, used to make the fit illustrated in Figure 3, the knock-ons and scintillation components are subsumed into a

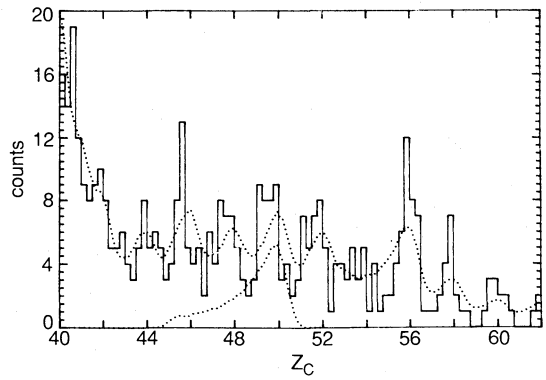

FIG. 9.—Charge histograms of particles in the $40 \leq Z \leq 62$ region. Smooth curve shows the results of fits with a three-component response function similar to that used in fitting the Fe as in Fig. 2.

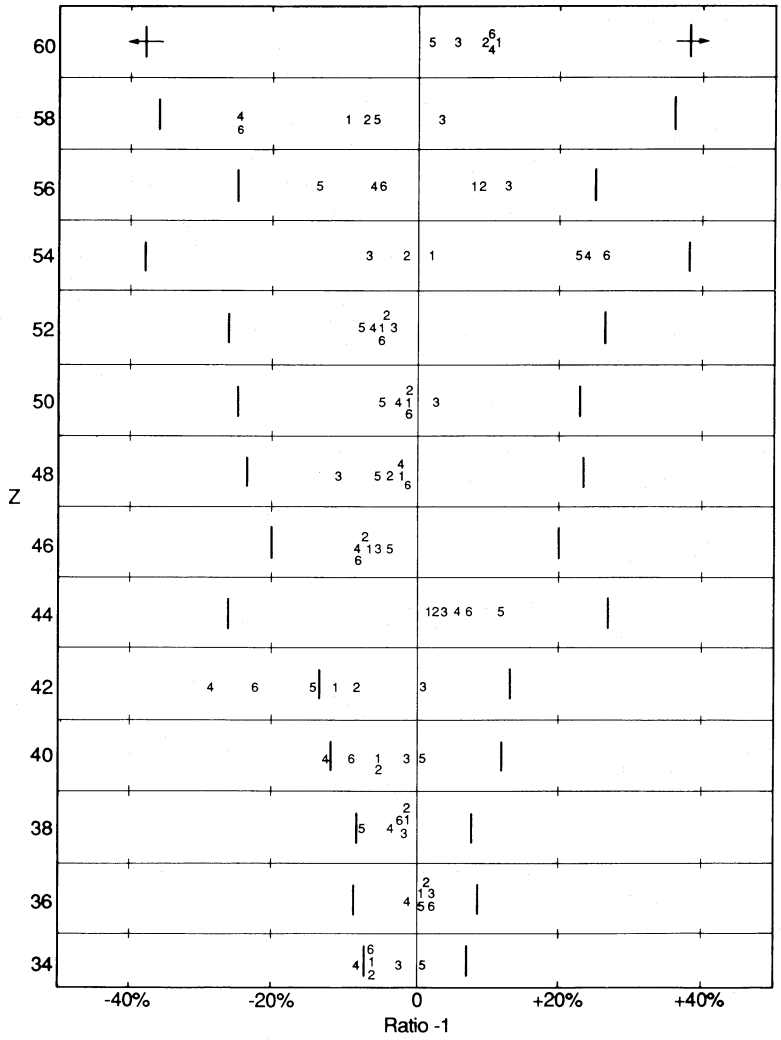

FIG. 10.—Ratios to adopted model for $34 \leq Z \leq 60$. Fractional deviations of abundances derived from various deconvolutions, compared with those derived from the adopted deconvolution as a function of charge. Points are shown as numbers which refer to the list of models below. Vertical bars show the statistical uncertainty for comparison. In the following list, Φ is the force field parameter, and n is the effective index of refraction as discussed in the text. Model 1, $\Phi = 0.6$ GV, $n = 1.518$, one component; Model 2, $\Phi = 0.3$ GV, $n = 1.518$, one component; Model 3, $\Phi = 0.6$ GV, three-component, saturation at $\gamma = 9.0$; Model 4, $\Phi = 0.6$ GV, $n = 2.00$, one-component; Model 5, $\Phi = 0.6$ GV, $n = 2.00$, one-component, 0.25 charge unit shift; Model 6, $\Phi = 0.6$ GV, $n \propto Z$, one component. The adopted model is described in the Appendix; it has $\Phi = 0.45$ GV, $n = 1.55$, and one-component Cherenkov light.

pure, one-component, Cherenkov model with an effective index of refraction ($n = 1.55$) applicable at these energies. The abundances quoted in Table 1 are based on this fit. However, we have considered a variety of fitting functions. We find that the abundances of element pairs are not very sensitive to reasonable variations in the index of refraction, or to other models we considered. Variations of fit abundances, relative to the abundances from the selected fit, are shown in Figure 10, and rms values of these variations were used to assign the systematic uncertainties to the abundances in Table 1.

In addition, the data appear to have peaks which are offset from integer values. The fit functions also show these offsets, due to the difference in assumed energy spectra for primaries and secondaries. The degree of offset seen in the fit functions for any particular element depends strongly on the assumed spectral shape, and on the Cherenkov response function. For the fit shown in Figure 3, we have shifted the peaks according to the secondary fractions, as given by Newport, rather than by adjusting the energy spectrum. While the shifts have dramatic effects on the peak to valley ratio and the appearance of the fit, they have very little effect on the abundances of even-odd element pairs.

As one would expect from the obvious quality of the data in the histogram in Figure 3, the abundances are not very sensitive to the deconvolution procedure. The rms deviation in the abundances, derived from a variety of fit functions with tails (with and without a knock-on component, with and without peak shifts, and with various refractive indices), is 8% (see Fig. 10). If we compare models with tails to Gaussian models, then we find a rms deviation of about 15%. The systematic uncertainties appear to be small compared to the statistical uncertainties for all abundances, with the exception of $Z = 41$, 42, and $Z = 33$, 34, which are not very well resolved. Since we find the Gaussian models implausible, we estimate no more than 8% standard deviation for the systematic uncertainties. The fitting functions which have tails, and therefore overlap adjacent elements, do have larger statistical uncertainties than were calculated for the non-overlapping Gaussian fit functions.

REFERENCES

Anders, E., and Ebihara, M. 1982, *Geochim Cosmochim. Acta*, **46**, 2363.
Anders, E., and Grevesse, N. 1989, *Geochim. Cosmochim. Acta*, in press.
Binns, W. R., Brewster, N. R., Fixsen, D. J., Garrard, T. L., Israel, M. H., Klarmann, J., Newport, B. J., Stone, E. C., and Waddington, C. J. 1985, *Ap. J.*, **297**, 111.
Binns, W. R., Fickle, R. K., Garrard, T. L., Israel, M. H., Klarmann, J., Stone, E. C., and Waddington, C. J. 1981*a*, *Ap. J. (Letters)*, **247**, L115.
———. 1982, *Ap. J. (Letters)*, **261**, L117.
Binns, W. R., Fickle, R. K., Garrard, T. L., Israel, M. H., Klarmann, J., Krombel, K. E., Stone, E. C., and Waddington, C. J. 1983*a*, *Ap. J. (Letters)*, **267**, L93.
Binns, W. R., Garrard, T. L., Israel, M. H., Jones, Michael D., Kamionkowski, M. P., Klarmann, J., Stone, E. C., and Waddington, C. J. 1988, *Ap. J.*, **324**, 1106.
Binns, W. R., Grossman, D. P., Israel, M. H., Jones, Michael D., Klarmann, J., Garrard, T. L., Stone, E. C., Fickle, R. K., and Waddington, C. J. 1983*b*, *Proc. 18th Internat. Cosmic Ray Conf. (Bangalore)*, **9**, 106.
Binns, W. R., Israel, M. H., Klarmann, J., Scarlett, W. R., Stone, E. C., and Waddington, C. J. 1981*b*, *Nucl. Instr. Meth.*, **185**, 415.
Breneman, H. H., and Stone, E. C. 1985, *Ap. J. (Letters)*, **299**, L57.
Brewster, N. R. 1984, Ph.D. thesis, University of Minnesota.
Brewster, N. R., Freier, P. S., and Waddington, C. J. 1983, *Ap. J.*, **264**, 324.
———. 1985, *Ap. J.*, **294**, 419.
Cameron, A. G. W. 1973, Space Sci. Rev., **15**, 121.
———. 1982*a*, *Essays in Nuclear Astrophysics*, ed. C. A. Barnes, D. D. Clayton, and D. N. Schramm (Cambridge: Cambridge University Press), p. 23.
———. 1982*b*, *Ap. Space Sci.*, **82**, 123.
Engelmann, J. J., *et al.* 1983, *Proc. 18th Internat. Cosmic Ray Conf. (Bangalore)*, **2**, 17.
Fowler, P. H., Walker, R. N. F., Masheder, M. R. W., Moses, R. T., Worley, A., and Gay, A. M. 1987, *Ap. J.*, **314**, 739.
Garrard, T. L., *et al.* 1983, *Proc. 18th Internat. Cosmic Ray Conf. (Bangalore)*, **9**, 367.
Gleeson, L. J., and Axford, W. I. 1968, *Ap. J.*, **154**, 1011.
Grevesse, N., and Meyer, J. P. 1985, *Proc. 19th Internat. Cosmic Ray Conf. (La Jolla)*, **3**, 5.
Israel, M. H. 1986, in *Proc. 12th Texas Symposium on Relativistic Astrophysics*, ed. M. Livio and G. Shaviv (*Ann. N.Y. Acad. Sci.*, **470**, 188).
Klarmann, J., *et al.* 1983, *Proc. 18th Internat. Cosmic Ray Conf. (Bangalore)*, **2**, 220.
Klarmann, J., Waddington, C. J., Binns, W. R., Garrard, T. L., Gibner, P. S., and Israel, M. H. 1987, *Proc. 20th Internat. Cosmic Ray Conf. (Moscow)*, **2**, 390.
Letaw, J. R., Silberberg, R., and Tsao, C. H. 1984, *Ap. J.*, **279**, 144.
Lezniak, J. A. 1976, *Nucl. Instr. Meth.*, **136**, 299.
Margolis, S. H. 1983, *Proc. 18th Internat. Cosmic Ray Conf. (Bangalore)*, **9**, 267.
Margolis, S. H., and Blake, J. B. 1985, *Ap. J.*, **299**, 334.
Meyer, J. P. 1985, *Proc. 19th Internat. Cosmic Ray Conf. (La Jolla)*, **9**, 141.
Newport, B. J. 1986, Ph.D. thesis, California Institute of Technology.
Ormes, J. F., and Protheroe, R. J. 1983, *Ap. J.*, **272**, 756.
Schramm, D. N. 1982, in *Essays in Nuclear Astrophysics*, ed. C. A. Barnes, D. D. Clayton, and D. N. Schramm (Cambridge: Cambridge University Press), p. 325.
Silberberg, R., and Tsao, C. H. 1973*a*, *Ap. J. Suppl.*, **25**, 315.
———. 1973*b*, *Ap. J. Suppl.*, **25**, 335.
Silberberg, R., Tsao, C. H., Letaw, J. R., and Shapiro, M. M. 1983, *Phys. Rev. Letters*, **51**, 1217.
Stone, E. C., *et al.* 1983, *Proc. 18th Internat. Cosmic Ray Conf. (Bangalore)*, **9**, 115.
Stone, E. C., *et al.* 1987, *Proc. 20th Internat. Cosmic Ray Conf. (Moscow)*, **1**, 366.
Waddington, C. J., Binns, W. R., Cummings, J. R., Garrard, T. L., Gibner, P. S., Israel, M. H., Kertzman, M. P., and Klarmann, J. 1987*a*, *Proc. 20th Internat. Cosmic Ray Conf. (Moscow)*, **2**, 149.
Waddington, C. J., Binns, W. R., Garrard, T. L., Israel, M. H., Kertzman, M. P., Klarmann, J., and Stone, E. C. 1987*b*, *Proc. 20th Internat. Cosmic Ray Conf. (Moscow)*, **2**, 152.
Webber, W. R. 1983, in *Composition and Origin of Cosmic Rays*, ed. M. M. Shapiro (Dordrecht: Reidel), p. 25.

W. R. BINNS, M. H. ISRAEL, and J. KLARMANN: Department of Physics and the McDonnell Center for Space Sciences, Washington University, St. Louis, MO 63130

T. L. GARRARD, P. S. GIBNER, and E. C. STONE: 220-47 Downs Laboratory, California Institute of Technology, Pasadena, CA 91125

M. P. KERTZMAN: Department of Physics and Astronomy, Depauw University, Greencastle, IN 46135

B. J. NEWPORT: Department of Physics, University of Utah, Salt Lake City, UT 84112

C. J. WADDINGTON: School of Physics and Astronomy, University of Minnesota, 116 Church St. S. E., Minneapolis, MN 55455